

Article

Iron-Doped Monoclinic Strontium Iridate as a Highly Efficient Oxygen Evolution Electrocatalyst in Acidic Media

Mengjie Li ¹, Jiabao Ding ¹, Tianli Wu ^{1,*}  and Weifeng Zhang ^{1,2,*}¹ Henan Key Laboratory of Photovoltaic Materials, Henan University, Kaifeng 475004, China² Center for Topological Functional Materials, Henan University, Kaifeng 475004, China

* Correspondence: tianliwu@henu.edu.cn (T.W.); wfzhang@henu.edu.cn (W.Z.)

Abstract: Ir-based perovskite oxides are efficient electrocatalysts for anodic oxygen evolution. This work presents a systematic study of the doping effects of Fe on the OER activity of monoclinic SrIrO₃ to reduce the consumption of Ir. The monoclinic structure of SrIrO₃ was retained when the Fe/Ir ratio was less than 0.1/0.9. Upon further increases in the Fe/Ir ratio, the structure of SrIrO₃ changed from a 6H to 3C phase. The SrFe_{0.1}Ir_{0.9}O₃ had the highest activity among the investigated catalysts with the lowest overpotential of 238 mV at 10 mA cm⁻² in 0.1 M HClO₄ solution, which could be attributed to the oxygen vacancies induced by the Fe dopant and the IrO_x formed upon the dissolution of Sr and Fe. The formation of oxygen vacancies and uncoordinated sites at the molecular level may be responsible for the improved performance. This work explored the effect of Fe dopants in boosting the OER activity of SrIrO₃, thus providing a detailed reference to tune perovskite-based electrocatalyst by Fe for other applications.

Keywords: perovskite oxides; dopant; electrocatalyst; oxygen evolution reaction



Citation: Li, M.; Ding, J.; Wu, T.; Zhang, W. Iron-Doped Monoclinic Strontium Iridate as a Highly Efficient Oxygen Evolution Electrocatalyst in Acidic Media. *Nanomaterials* **2023**, *13*, 797. <https://doi.org/10.3390/nano13050797>

Academic Editor: Justo Lobato

Received: 31 January 2023

Revised: 15 February 2023

Accepted: 20 February 2023

Published: 22 February 2023



Copyright: © 2023 by the authors. Licensee MDPI, Basel, Switzerland. This article is an open access article distributed under the terms and conditions of the Creative Commons Attribution (CC BY) license (<https://creativecommons.org/licenses/by/4.0/>).

1. Introduction

The energy crisis is an important issue that needs to be solved urgently in modern society. Energy consumption and overuse of fossil fuels contribute to global warming and climate change. Hydrogen energy carriers offer a potential way to solve this challenge, [1,2] and water splitting can produce hydrogen and uses the hydrogen evolution reaction (HER) at the cathode and oxygen evolution reaction (OER) at the anode [3–5]. Unlike the hydrogen reaction at the cathode, the half-reaction at the anode is sluggish due to the multi-proton/electron-coupled process, which usually plays a critical part in the total efficiency of the system [6–8]. Hence, substantial efforts have been dedicated to the exploration of efficient OER electrocatalysts to reduce the reaction barrier over the past decade [9–11]. Many electrocatalysts based on transition metals are effective for OER under base electrolyte, but only a few of the recently described electrocatalysts have been investigated for utilization in acidic solution due to their extremely corrosive condition [4,12,13]. Ruthenium (Ru)- and iridium (Ir)- based oxides are recognized as state-of-the-art catalysts for OER in acidic media [14]. Though the Ru-based oxides exhibit relatively lower overpotentials than the Ir-based oxides, their stabilities are limited under acidic conditions, [15] and their low abundance and high costs further limit industrialization. Hence, there is an urgent need for high-performance and stable catalysts that consume minimal Ir content.

In recent years, high-entropy materials have been fine-tuned due to their compositional flexibility, and high-entropy mixing provides structural stability under operating conditions. It has been proven to be a unique platform for designing surface composition and active sites, and developing efficient electrocatalysts for water splitting using the synergistic effect of multiple components [16]. Rutile ruthenium oxide (RuO₂) has strong oxygen-binding ability. Many reports have effectively adjusted the intrinsic electronic structure and the active site of the catalyst to produce defects by doping transition metals in RuO₂. Moreover,

the doped RuO₂ catalyst, combined with nanostructure and morphology engineering, performs significant enhanced mass activity and stability [17]. Perovskite oxides are widely used in various energy-related electrocatalyst fields due to their lower cost, flexible structure and high catalytic activity. It is an effective way to improve electrocatalytic performance of perovskites by reducing the size of large pieces to the nanoscale [18]. Perovskite-type oxides are usually defined by the formula ABO₃ and can accommodate a variety of cations, thus allowing the partial substitution of cations at the A sites or B sites. The transition metal at the B site of a perovskite oxide is the main catalytic center, which directly affects the catalytic performance of OER, making it easier to tune the electronic structure of a B-site metal ion of a perovskite oxide because of its unique electronic structures and flexible inter-ionic composition [19–21]. Ir-based perovskites, such as the SrIrO₃, have attracted great attention in studies of OER electrocatalysts due to their low cost and high activities in acidic media [6–8,22]. To further reduce the content of Ir in the perovskites and modulate their OER activities, transition metals can be introduced into the B site to boost perovskite performance because the d-orbitals provided by the transition metals favor binding oxygen species with optimal barriers. Moreover, iron (Fe) has played a critical role in the oxygen evolution of Ni-based electrocatalysts in alkaline electrolytes because it has numerous advantages including it being highly abundant, non-poisonous, and low in cost. To the best of our knowledge, there is a lack of systematic exploration of the effect of Fe on the OER activity of monoclinic SrIrO₃.

Here, we report Fe-doped monoclinic SrIrO₃ (named SrFe_xIr_{1-x}O₃) by a solid-state method at atmospheric pressure. The oxygen vacancies and high oxidation state of the Ir generated by the Fe dopant enhanced the OER activity of monoclinic SrIrO₃. The SrFe_{0.1}Ir_{0.9}O₃ exhibits the best OER activity among the investigated samples, and their mass activity at 1.52 V is 1.69-fold higher than that of SrIrO₃. During the electrochemical tests, amorphous planes successively form after the leaching of Sr and Fe, thus contributing to enhanced catalytic activity.

2. Materials and Methods

2.1. Materials Synthesis

The four polycrystalline SrFe_xIr_{1-x}O₃ samples studied in this work were synthesized by conventional solid-phase methods. Powder precursors were used: strontium carbonate (Aladdin Co., Ltd., Shanghai, China), iridium dioxide (Bairui Co., Ltd., Kunming, Yunnan, China) and ferric oxide (Aladdin, Co., Ltd., Shanghai, China). Four different ratios of SrFe_xIr_{1-x}O₃ were prepared by changing the ratio of Ir:Fe using Ir:Fe precursor ratios of 1:0.05, 1:0.1, 1:0.15, and 1:0.2. Stoichiometric strontium precursors were always added in a 1:1 ratio to total B-site precursors. The starting powder reagents were mixed, ground and preheated in air at 600 °C in an alumina crucible for 5 h. Then the obtained powder was pulverized, granulated, and calcined in air at 1100 °C for 24 h.

2.2. Electrochemical Measurements

All electrochemical measurements were performed in 0.1 M HClO₄ electrolyte. Inks were prepared by 2.5 mg of catalyst powder and 1 mg of carbon black in a liquid solution consisting of 470 μL of isopropanol and 30 μL of Nafion (Sigma-Aldrich, Shanghai, China, a 5% mixture of lower fatty alcohols and water). This ink was sonicated for 1 h immediately before dripping onto a polished glassy carbon electrode with an area of 0.071 cm² to obtain a catalyst loading of 0.85 mg cm⁻². A three-electrode system was used with a clean platinum sheet counter electrode and a saturated calomel electrode reference electrode. The cyclic voltammetry (CV) test was carried out at 0.1 M HClO₄ saturated with O₂ (scan rate 100 mV s⁻¹). The linear sweep voltammetry (LSV) test was carried out at a scan rate of 5 mV s⁻¹ with 85% iR-drop compensation, sweeping from 1.23 up to 1.59 V vs. RHE for the OER current measurements. To measure stability, chronopotentiometric measurements were made at a constant current density of 10 mA cm⁻². In the range of 0.4–1.3 V, a cyclic voltammetry (CV) test was performed at a scanning rate of 0.1 V s⁻¹ to study the redox

behavior of the electrocatalyst. To calculate the effective electrochemical active surface area (ECSA), the double-layer capacitance was measured in a non-faradaic potential range (1.136–1.236 V vs. RHE) by recording the current values as a function of scan rate and the scan rates were 10, 20, 40, 60, 80, and 100 mV s⁻¹. The double-layer capacitance (C_{dl}) was estimated by plotting the $\Delta j = (j_+ - j_-)/2$ at 1.186 V vs. RHE against the scan rate. The ECSA was estimated according to the following equation:

$$ECSA = \left(\frac{C_{dl}}{C_s} \right) (\text{cm}^2) \quad (1)$$

Calibration is performed by using a reversible hydrogen electrode (RHE). First, Pt electrodes were washed with 0.1 M HClO₄ cycling between -2 and 2 V for 1 h. It is then used as a working electrode and a counter electrode, respectively. Prior to calibration, the electrolyte 0.1 M HClO₄ should be continuously bubbled H₂ to saturate it with H₂. A series of potential control time-ampere curves of 500 s were measured, and the current interconversion between the hydroxide and hydrogen evolution reactions was obtained. The resulting potential is the potential of zero net current. In this work, a potential of zero net current was found at -0.286 V compared to the SCE electrode in 0.1 M HClO₄ (Figure S7). Therefore, Equation (2) can be used to convert the potential measured relative to SCE to the potential relative to RHE:

$$E_{vs.RHE} = E_{vs.SCE} + 0.286 \text{ V} \quad (2)$$

Faraday efficiency is calculated by the ratio of the amount of O₂ produced in the experiment to the actual value. The O₂ gas produced by the electrochemical reaction is collected by the drainage method, and then the number of moles of the O₂ produced is calculated according to the ideal gas law. The theoretical value is determined by assuming that 100% of the current output during the reaction is attributed to OER. According to theoretical considerations, the ratio of the amount of O₂ to the expected amount of O₂ is the Faraday efficiency.

The dissolution of catalyst in the OER process was determined by inductively coupled plasma optical emission spectrometry (ICP-OES, iCAP7400, Thermo Fisher, Waltham, MA, USA). The catalyst was loaded onto carbon paper with a catalyst load of about 1 mg cm⁻² and electrolyzed at 10 mA cm⁻². A small amount (10 mL) of electrolyte is used to meet the device's detection limits. Electrolyte was collected after 0.5 h, 1 h, 2 h, 4 h, 6 h, and 8 h electrolysis. At each sampling site, 4 mL electrolyte was removed for ICP measurements and replenished to 10 mL with clean electrolyte before the next sampling cycle. The stability number (S-number) was calculated using the following equation [23]:

$$S_{number} = \frac{n_{O_2}}{n_{Ir}} \quad (3)$$

2.3. Materials Characterization

Powder X-ray diffraction (XRD) patterns were collected on a Bruker D8 Advance X-ray diffractometer with a Cu K α radiation source ($\lambda = 1.5418 \text{ \AA}$). Transmission electron microscopy (TEM) images were collected on a JEM-F200 (JEOL, Tokyo, Japan). Scanning electron microscopy (SEM) images were studied in a JSM 7001F electron microscope at 10 kV. Energy dispersive X-ray analysis (EDXA) was performed using the EDXA system on a JSM-7610F scanning electron microscope. X-ray photoelectron spectroscopy (XPS) was performed on an AXIS SUPRA+ X-ray photoelectron spectrometer. Avantage software was used for peak fitting. The specific surface area was obtained using nitrogen adsorption on a Besorp-Max II (MicrotracBEL, Tokyo, Japan).

2.4. Electrochemical Measurements

Electrochemical workstations (CHI 660E, Chenhua Co., Shanghai, China) were used to analyze the HER polarization curves in 0.5 M H₂SO₄ at room temperature. A saturated calomel electrode (SCE) and graphite rod were used as the reference electrode and counter electrode, respectively. The SCE electrode was calibrated relative to the reversible hydrogen electrode (RHE). Linear sweep voltammetry (LSV) data were collected at a scanning rate of 2 mV s⁻¹. The time dependence of the catalytic current during the electrolysis of the catalyst in 0.5 M H₂SO₄ was measured at potentiostatic voltage.

3. Results and Discussion

Here, the Fe-doped monoclinic SrIrO₃ with different doping amounts was synthesized via a solid-state method at atmospheric pressure and named SrFe_xIr_{1-x}O₃. The SrFe_{0.1}Ir_{0.9}O₃ had the best catalytic activity for OER in 0.1 M HClO₄. The structures and morphologies of the SrFe_{0.1}Ir_{0.9}O₃ and SrIrO₃ were initially characterized by XRD, SEM, and TEM measurements. Figure 1a shows the XRD patterns of SrIrO₃ and SrFe_{0.1}Ir_{0.9}O₃. The diffraction peaks of SrFe_{0.1}Ir_{0.9}O₃ are similar to those of SrIrO₃ where the clear diffraction peaks correspond to lattice planes of monoclinic SrIrO₃ (JCPDS card no.72-0855), thus revealing a crystalline structure of SrIrO₃ after doping with Fe. Further comparisons of the XRD patterns show that the diffraction peaks of SrFe_{0.1}Ir_{0.9}O₃ shift to smaller diffraction locations than SrIrO₃, thus demonstrating a slight expansion of the perovskite framework after Fe doping. This phenomenon can be explained by the fact that the radius of Fe³⁺ ions (65 pm) is larger than that of Ir⁴⁺ ions (63 pm). Figure S1 shows that the XRD pattern of SrFe_{0.05}Ir_{0.95}O₃ has a similar diffraction peak as SrFe_{0.1}Ir_{0.9}O₃ and SrIrO₃, which exhibits less of a shift toward the lower position of diffraction peaks than SrFe_{0.1}Ir_{0.9}O₃ versus SrIrO₃. When the Fe/Ir ratio increased to 0.15/0.85 and 0.2/0.8, the locations of the main peaks showed a greater shift toward lower angles versus SrFe_{0.1}Ir_{0.9}O₃.

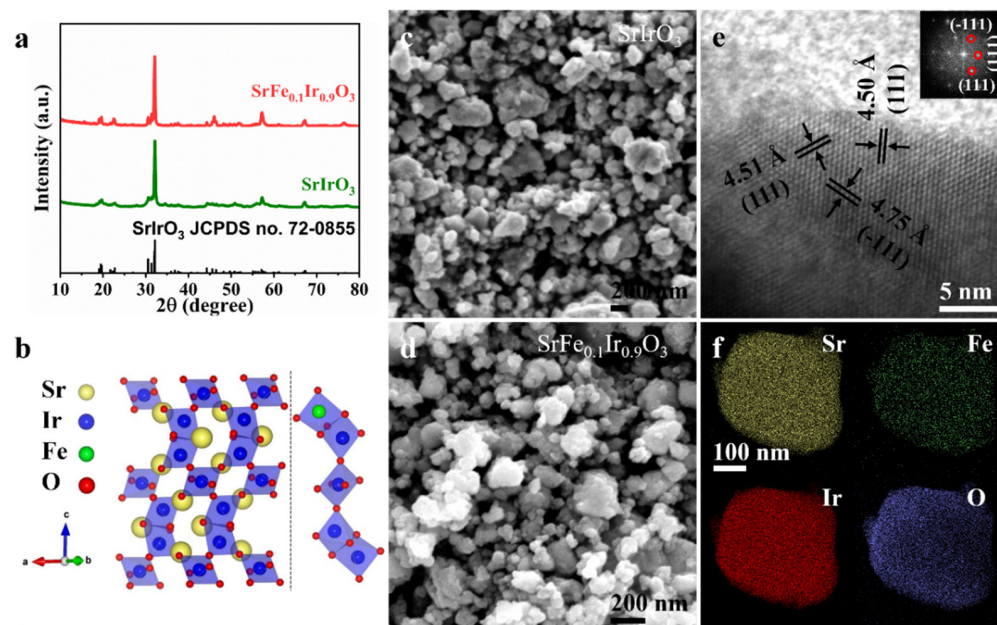


Figure 1. (a) XRD patterns of SrFe_{0.1}Ir_{0.9}O₃ and SrIrO₃. (b) Crystal structure of SrIrO₃ and the proposed Fe-doped local connection pattern of IrO₆ octahedra in monoclinic SrFe_{0.1}Ir_{0.9}O₃. (c) SrIrO₃ and (d) SrFe_{0.1}Ir_{0.9}O₃. (e) HRTEM image captured from SrFe_{0.1}Ir_{0.9}O₃. Inset: the corresponding fast Fourier transform image. (f) The elemental mapping images of a typical nanoparticle of SrFe_{0.1}Ir_{0.9}O₃.

The crystal structure gradually transforms from a 6H phase to a 3C phase perovskite structure upon a gradual increase in the Fe content (Figure S1), which is consistent with the literature [24]. The left part of Figure 1b shows the typical crystal structure of monoclinic

SrIrO₃ that consists of alternating face-sharing IrO₆ octahedra dimers and corner-sharing IrO₆ octahedra along the c-axis. Previous studies show that the Ir-O bond in the coplanar IrO₆ octahedral dimer is significantly weaker than that in the angle-sharing isolated octahedron. Fe atoms are more inclined to substitute the Ir atoms on the IrO₆ octahedral dimer shared by the faces (right part in Figure 1b) [25]. The higher valence state of Ir is increased by the redistribution of electrons from Ir to Fe atoms due to the large number of Fe atoms in the crystal lattice. Different Fe contents have a great influence on the Ir-O bonding electron environment, and the electron orbital hybridization is more complicated. As the iron content increases, lattice distortion which leads to the phase transitions would occur violently in polygon octahedral dimers. The inherent electronic structure and the high valence state of Ir atom contribute to its high catalytic activity and good stability, respectively, thereby optimizing the water dissociation kinetics [26]. The SEM images of SrIrO₃ and SrFe_{0.1}Ir_{0.9}O₃ show that both SrIrO₃ and SrFe_{0.1}Ir_{0.9}O₃ are composed of granular, micron-sized particles, and the size of SrFe_{0.1}Ir_{0.9}O₃ nanoparticles become larger (Figure 1c,d). The corresponding Brunauer–Emmett–Teller (BET) surface areas of the above two samples are also provided. SrFe_{0.1}Ir_{0.9}O₃ has a lower BET value due to its larger particle size than SrIrO₃ (Figure S2). The atomic ratios of SrIrO₃ and SrFe_{0.1}Ir_{0.9}O₃ were collected by energy dispersive X-ray spectroscopy (EDX), thus showing the existence of the corresponding elements (Figure S3). Figure 1e shows a high-resolution TEM image of an SrFe_{0.1}Ir_{0.9}O₃ nanoparticle. The top-right corner is the corresponding fast Fourier transform (FFT) image. Three groups of lattice fringes with interplanar distances of 4.50 Å, 4.51 Å, and 4.75 Å correspond to the (111), (111), and (−111) crystallographic planes of SrFe_{0.1}Ir_{0.9}O₃, respectively. Figure 1f shows the elemental mapping images of SrFe_{0.1}Ir_{0.9}O₃ of a representative nanoparticle including even distributions of Sr, Fe, Ir, and O via TEM and high-angle annular dark-field scanning TEM. The elemental distribution of SrIrO₃ is shown in Figure S4.

To investigate the modulation effect of Fe on the OER activity of SrIrO₃, the electrocatalytic OER performance of SrFe_xIr_{1-x}O₃ was evaluated upon comparison with pristine SrIrO₃. The electrochemical measurements of SrIrO₃ and SrFe_xIr_{1-x}O₃ samples were evaluated in 0.1 M HClO₄ at room temperature using a three-electrode system. Figure 2a shows the 85%IR-corrected polarization curves of SrFe_xIr_{1-x}O₃ and SrIrO₃ normalized by geometric area at a scan rate of 5 mV s^{−1}. Versus SrIrO₃, the SrFe_{0.1}Ir_{0.9}O₃ and SrFe_{0.05}Ir_{0.85}O₃ showed higher catalytic activities than that of SrIrO₃. At a current density of 10 mA cm^{−2}, the overpotential of SrFe_{0.1}Ir_{0.9}O₃ is 238 mV, which is much lower than that of SrIrO₃ (256 mV) (Figure 2b). The Tafel slopes of the samples derived from the polarization curves are shown in Figure 2c and show the lowest Tafel slope of SrFe_{0.1}Ir_{0.9}O₃ (52.5 mV dec^{−1}) among the investigated catalysts. The SrFe_{0.1}Ir_{0.9}O₃ exhibits a low overpotential and Tafel slope, which are even lower than most of the perovskite oxides (Table S1). The exchange current densities of SrFe_xIr_{1-x}O₃ and SrIrO₃ also confirm the highest activity of SrFe_{0.1}Ir_{0.9}O₃ (Figure S5). The currents were normalized with the mass of Ir to carefully evaluate the performance of SrFe_{0.1}Ir_{0.9}O₃. The results show that SrFe_{0.1}Ir_{0.9}O₃ has higher activity than SrIrO₃ (Figure 2d). It is clear that the estimated mass activity of SrFe_{0.1}Ir_{0.9}O₃ at an overpotential of 290 mV is close to 79.1 A g_{Ir}^{−1}. This value is 1.69-fold higher than that of SrIrO₃ (46.6 A g_{Ir}^{−1}). The electrochemical surface area (ECSA) of the samples was estimated from the double-layer capacitance. The ECSA-normalized current density of SrFe_{0.1}Ir_{0.9}O₃ and SrIrO₃ were also evaluated (Figure 2d). The ECSA-normalized current of SrFe_{0.1}Ir_{0.9}O₃ at 1.52 V (vs. RHE) is 1.67-fold higher than that of SrIrO₃, thus indicating the better activity of SrFe_{0.1}Ir_{0.9}O₃ than that of SrIrO₃. To further evaluate the intrinsic activity of catalysts, the currents were normalized by the BET surface areas illustrating the higher catalytic activity of SrFe_{0.1}Ir_{0.9}O₃ than SrIrO₃ (Figure S6). The Faradaic efficiency of oxygen evolution for SrFe_{0.1}Ir_{0.9}O₃ (Figure 2e) illustrates the correlation between time and oxygen production at a current of 10 mA where almost all electrons were transferred toward oxygen evolution. The stability of SrFe_{0.1}Ir_{0.9}O₃ and SrIrO₃ was further examined by galvanostatic measurements. Figure 2f shows the slight potential change during the entire period for

$\text{SrFe}_{0.1}\text{Ir}_{0.9}\text{O}_3$ at a geometrical current density of 10 mA cm^{-2} , thus illustrating the high stability of $\text{SrFe}_{0.1}\text{Ir}_{0.9}\text{O}_3$.

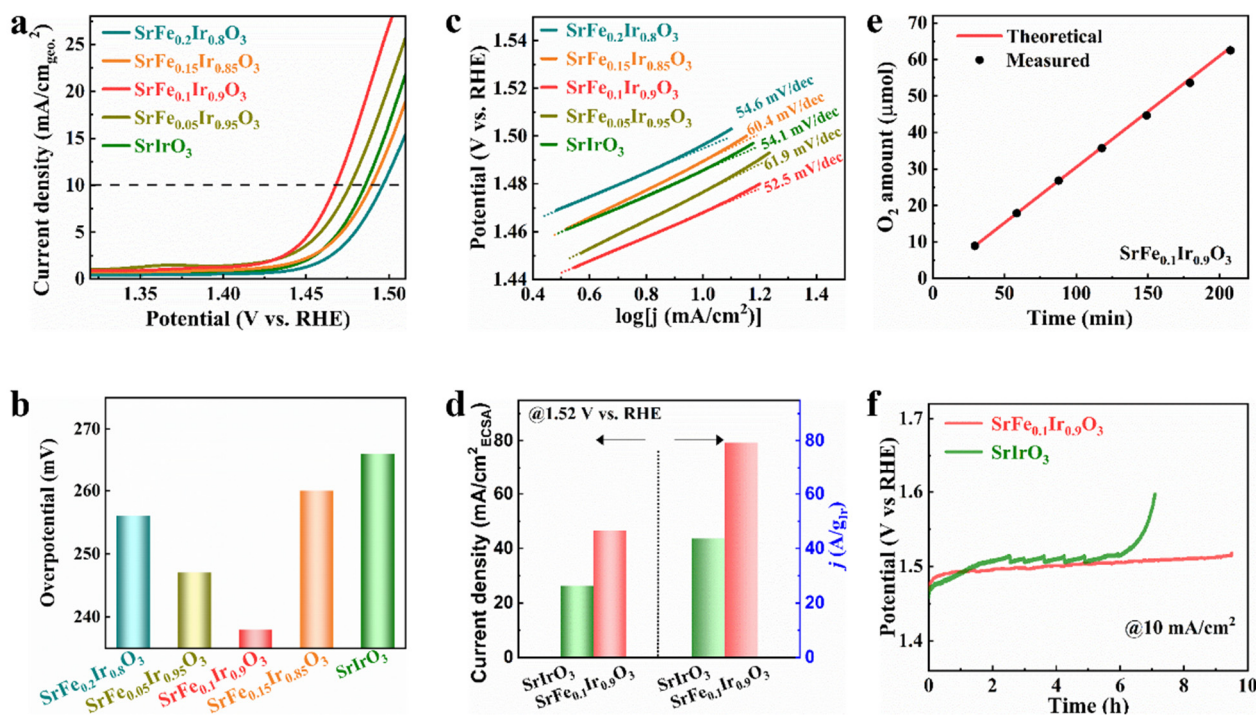


Figure 2. (a) Polarization curves of SrIrO_3 and $\text{SrFe}_x\text{Ir}_{1-x}\text{O}_3$ normalized by geometric area in 0.1 M HClO_4 solution with 85% IR compensations. (b) Overpotentials of SrIrO_3 and $\text{SrFe}_x\text{Ir}_{1-x}\text{O}_3$ at 10 mA cm^{-2} in 0.1 M HClO_4 solution. (c) The Tafel slope of the samples in (a). (d) ECSA and iridium amount normalized current density of SrIrO_3 and $\text{SrFe}_{0.1}\text{Ir}_{0.9}\text{O}_3$ at 1.52 V. (e) The amount of O_2 theoretically calculated and experimentally measured in the presence of $\text{SrFe}_{0.1}\text{Ir}_{0.9}\text{O}_3$ versus time at a current density of mA cm^{-2} . (f) Chronopotentiometric curve of $\text{SrFe}_{0.1}\text{Ir}_{0.9}\text{O}_3$ and SrIrO_3 in 0.1 M HClO_4 solution at 10 mA cm^{-2} for OER.

The XPS measurements were performed to investigate the chemical states of $\text{SrFe}_{0.1}\text{Ir}_{0.9}\text{O}_3$ and SrIrO_3 . Compared to the Ir 4f XPS spectrum of SrIrO_3 , the binding energies (62.5 eV and 65.5 eV) corresponding to Ir 4f_{7/2} and Ir 4f_{5/2} for the $\text{SrFe}_{0.1}\text{Ir}_{0.9}\text{O}_3$ are at higher values, thus suggesting that the average oxidation state of Ir in $\text{SrFe}_{0.1}\text{Ir}_{0.9}\text{O}_3$ is higher than 4⁺ and regulates the charge caused by the introduction of Fe (Figure 3a). Figure 3b shows the Fe 2p XPS spectra of SrIrO_3 and $\text{SrFe}_{0.1}\text{Ir}_{0.9}\text{O}_3$. The intensity of the Fe 2p peak is very weak, thus indicating a lower Fe content on the surface of $\text{SrFe}_{0.1}\text{Ir}_{0.9}\text{O}_3$. The two satellite peaks of high-resolution Fe 2p XPS at 710.9 eV and 724.4 eV can be assigned to Fe³⁺. Figure 3c shows that the O 1s XPS spectra of SrIrO_3 and $\text{SrFe}_{0.1}\text{Ir}_{0.9}\text{O}_3$ are divided into four peaks: lattice oxygen (528.5 eV, 529.7 eV), oxygen vacancy (530.95 eV), and adsorbed water (532.35 eV) [27,28]. According to the literature, higher vacancy concentrations and oxidation states of Ir result in more electrophilic catalysts, thus increasing the deprotonation rate to accelerate the OER reaction [29].

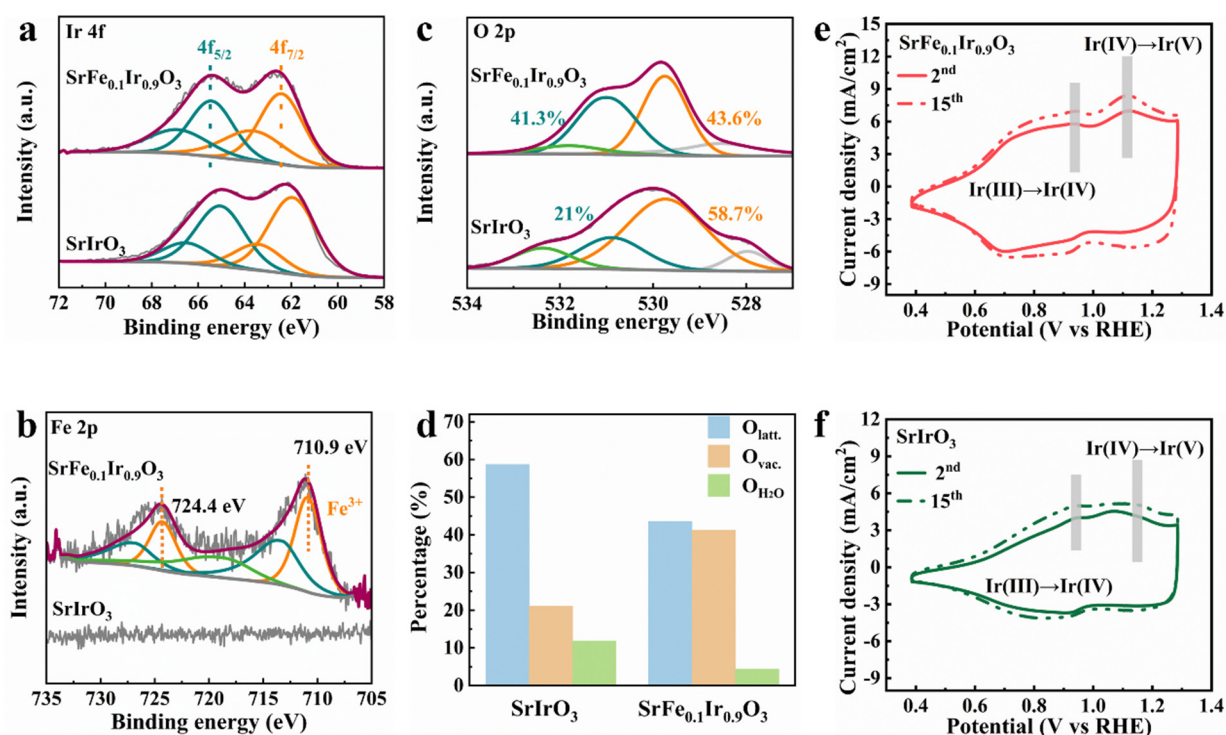


Figure 3. (a) Ir 4f, (b) Fe 2p, and (c) O 2p XPS spectra of SrIrO₃ and SrFe_{0.1}Ir_{0.9}O₃. (d) Result of O 1s orbital XPS spectra of SrIrO₃ and SrFe_{0.1}Ir_{0.9}O₃. The cyclic voltammetry (CV) curves recorded at the 2nd and 15th cycles for (e) SrIrO₃ and (f) SrFe_{0.1}Ir_{0.9}O₃.

Figure 3d shows the content of different oxygen species in which the content of oxygen vacancies or hydroxyl groups in SrFe_{0.1}Ir_{0.9}O₃ is about 20% higher than that of SrIrO₃, thus facilitating oxygen species absorption/desorption [30–32]. For some compounds, these vacancies are related to the overall catalytic performance. For instance, oxygen vacancies appear when the host and guest atoms have different oxidation states in SrFeO₃ [33]. Most perovskite materials have a propensity for oxygen vacancies due to solid-phase methods at high temperatures, which leads to the distortion of the oxygen octahedron [34]. The oxygen deficiency is closely related to the bond covalency of M–O and catalytic activity. From the perspective of the adsorption evolution mechanism, the increase in covalency leads to an increase in the electron density of the Ir site and a decrease in the electrostatic interaction with the oxygen intermediate species, thus weakening the binding energy of Ir to the oxygen intermediate species [35–37].

Similarly, the Ir–O bond length shortens as the covalent degree increases, which is favorable for the formation of electrophilic oxygen intermediates. Here, the electrophilicity of the oxygen intermediate species is also enhanced and can facilitate the nucleophilic attack of water molecules. Upon the introduction of oxygen vacancies, the valence state of metal ions changes, thus forming more covalent Fe–O bonds [38,39]. Considering that the Ir species with different oxidation states are highly correlated with electrocatalytic activity, we investigated the redox behavior of SrFe_{0.1}Ir_{0.9}O₃ and SrIrO₃ by cyclic voltammetry cycles. Figure 3e,f show that their 2nd and 15th redox curves were collected. Two oxidation peaks can be observed in their CV plots, thus representing Ir³⁺/Ir⁴⁺ and Ir⁴⁺/Ir⁵⁺, respectively. The redox of SrIrO₃ is mainly Ir³⁺/Ir⁴⁺. However, Ir⁴⁺ is easily oxidized to Ir⁵⁺ for SrFe_{0.1}Ir_{0.9}O₃. Ir⁵⁺ can serve as an active intermediate during the OER process: it increases the OER activity. Therefore, the good activity of SrFe_{0.1}Ir_{0.9}O₃ can be attributed to the easier generation of the active intermediate Ir⁵⁺. The fitting results of SrFe_{0.1}Ir_{0.9}O₃ and SrIrO₃ are listed in Table S2.

Next, to study the stability of the catalyst, the structure of SrFe_{0.1}Ir_{0.9}O₃ was investigated by XRD, HRTEM, and XPS after a 10 h durability test. The XRD pattern of

$\text{SrFe}_{0.1}\text{Ir}_{0.9}\text{O}_3$ after the stability test has similar diffraction peaks as the $\text{SrFe}_{0.1}\text{Ir}_{0.9}\text{O}_3$ before testing, thus revealing that it retains the main structure (Figure 4a). The HRTEM image captured from $\text{SrFe}_{0.1}\text{Ir}_{0.9}\text{O}_3$ after durability measurements indicates that the surface structure reconstruction occurs during electrochemical processes. The surface region with a depth of about 5–7 nm becomes amorphous, while the body of the $\text{SrFe}_{0.1}\text{Ir}_{0.9}\text{O}_3$ retains its initial crystalline structure. This confirms the XRD data. The cation leaching amount in OER process was quantitatively determined by inductively coupled plasma atomic emission spectrometry (ICP–OES) [40]. As shown in Figure S8, for $\text{SrFe}_{0.1}\text{Ir}_{0.9}\text{O}_3$, the amount of Sr and Fe in the electrolyte was detected to increase for a short time and then level off. The existence of the amorphous state on the surface indicates that a large amount of Sr and Fe dissolved into the solution, and IrO_x formed on the surface. The corrosion of Sr and Fe exposes more active sites on the surface of the catalyst, which further enhances its catalytic activity. Figure 4c is the Ir 4f XPS spectrum of $\text{SrFe}_{0.1}\text{Ir}_{0.9}\text{O}_3$ before and after durability testing, thus showing the positive shift of binding energies by approximately 0.4 eV after the stability test, which can be attributed to the formation of high-valence Ir.

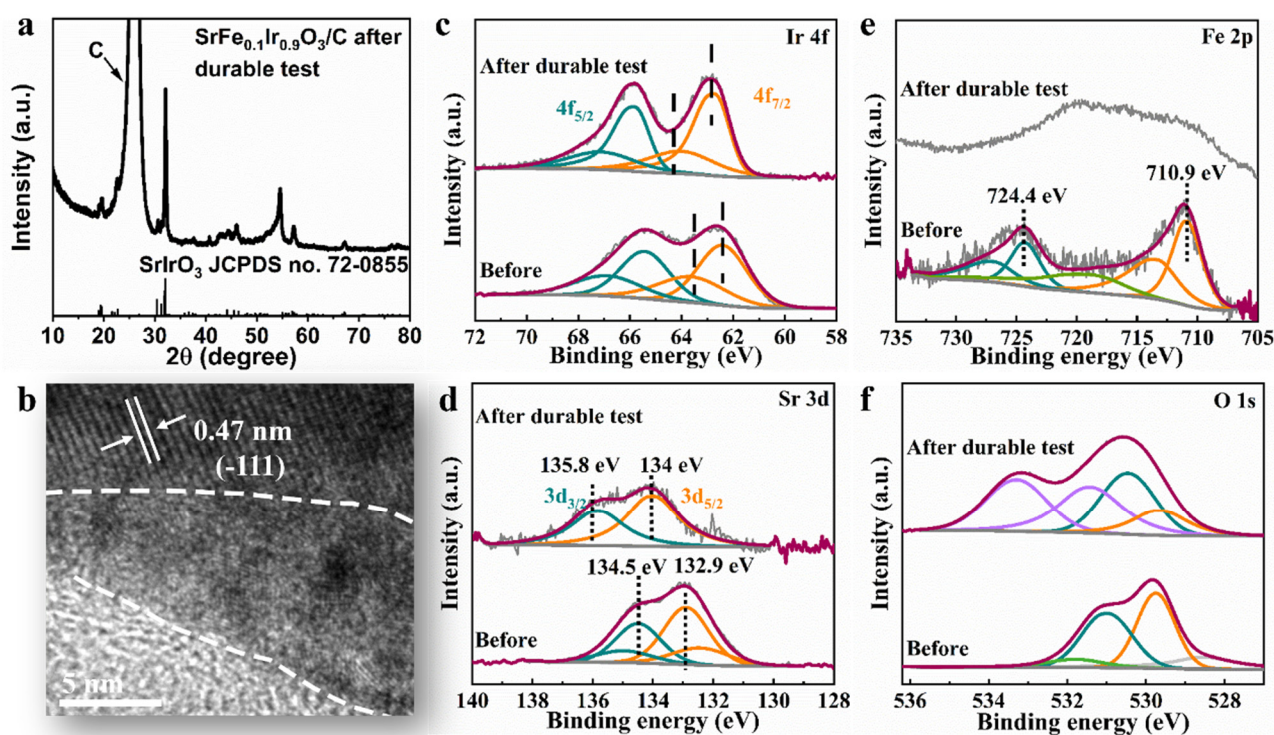


Figure 4. (a) XRD pattern of $\text{SrFe}_{0.1}\text{Ir}_{0.9}\text{O}_3/\text{C}$ after a 10 h durability test, (b) HRTEM image of $\text{SrFe}_{0.1}\text{Ir}_{0.9}\text{O}_3$ after a 10 h durability test. (c) Ir 4f, (d) Sr 3d, (e) Fe 2p, and (f) O 2p XPS spectra of $\text{SrFe}_{0.1}\text{Ir}_{0.9}\text{O}_3$ before and after 10 h durability test.

The fitting parameters for the Ir 4f XPS spectrum of $\text{SrFe}_{0.1}\text{Ir}_{0.9}\text{O}_3$ are listed in Supplementary Table S3. The Ir 4f peak from the second doublet has an energy shift of 1.6 eV, which is much larger than that observed in the pristine sample (~ 1.0 eV). This indicates that the surface structure of IrO_6 becomes more complex. Figure 4d shows the Sr 3d XPS data for $\text{SrFe}_{0.1}\text{Ir}_{0.9}\text{O}_3$ initially and after the durability testing, thus revealing a significant reduction in the Sr of $\text{SrFe}_{0.1}\text{Ir}_{0.9}\text{O}_3$ due to the leaching of Sr from the surface into the electrolyte. The peak positions at the binding energies of 132.9 eV and 134.5 eV are attributed to the lattice Sr in the perovskite. After the durability testing, part of the lattice Sr was converted to surface Sr.

Figure 4e shows that the Fe 2p XPS spectrum has peaks at 710.9 and 724.4 eV, which can be assigned to Fe^{3+} . After the OER test, the signal of Fe^{3+} is almost invisible, thus indicating the dissolution of Fe into the electrolyte. Similarly, the positive shift of binding energies

is observed in the O 1s XPS spectrum of SrFe_{0.1}Ir_{0.9}O₃ after durability testing (Figure 4f). The dissolution of the non-precious metal Fe and the precipitation of Sr introduces a large number of cationic vacancies. When cationic vacancies exist, the content of oxygen species is greatly increased to confirm a charge balance and promote nucleophilic attack of water and the formation of OOH* species [32]. The coordination of oxygen is unsaturated due to the existence of surface defects, which is easy to combine with protons to form surface hydroxyl species [41]. Hydroxyl species are active intermediates on the active sites, and the increase in number of active sites on the catalyst surface further improves the oxygen evolution activity of the samples.

4. Conclusions

In this study, it was found that Fe-doped monoclinic SrIrO₃ with Fe/Ir ratios of 0.05/0.95, 0.1/0.9, 0.15/0.85, and 0.2/0.8 were successfully synthesized by a solid-phase reaction. When the Fe/Ir ratio was 0.1/0.9, the monoclinic structure was retained after Fe doping. Further increases in the Fe/Ir ratio to 0.15/0.85 and 0.2/0.8 led to an SrIrO₃ change from 6H to 3C. The SrFe_{0.1}Ir_{0.9}O₃ exhibited the best activity for OER among the investigated samples with an overpotential of 238 mV at 10 mA cm⁻², which was much lower than that of SrIrO₃. The oxygen vacancies induced by the Fe dopants contributed to the enhanced OER activity of SrFe_{0.1}Ir_{0.9}O₃. The SrFe_{0.1}Ir_{0.9}O₃ catalyst has high activity and good stability, and this work provides a reference for the design of non-noble metal-doped high-efficiency acid water oxidation electrocatalysts to further improve the utilization efficiency of precious metal iridium.

Supplementary Materials: The following supporting information can be downloaded at: <https://www.mdpi.com/article/10.3390/nano13050797/s1>. Figure S1: XRD patterns of SrIrO₃ and SrFe_xIr_{1-x}O₃; Figure S2: N₂ adsorption-desorption isotherms of (a) SrIrO₃ and (b) SrFe_{0.1}Ir_{0.9}O₃. The graph provides the BET surface area; Figure S3: Energy Dispersive X-ray Spectroscopy (EDX) Study of (a) SrIrO₃ (b) and SrFe_{0.1}Ir_{0.9}O₃; Figure S4: The corresponding elemental mapping image of SrIrO₃ (scale bar, 100 nm); Figure S5: Exchange current density of SrIrO₃ and SrFe_xIr_{1-x}O₃ at 10 mA/cm²_{geo} in 0.1 M HClO₄ solution; Figure S6: Comparisons of current densities normalized by BET surface areas for SrIrO₃ and SrFe_{0.1}Ir_{0.9}O₃; Figure S7: The current as a function of the applied potentials for the calibration of SCE reference electrode; Figure S8: Contents of leached metals in the electrolyte in the presence of SrFe_{0.1}Ir_{0.9}O₃ during 8 h long electrocatalysis. Table S1: Comparison of OER activities for the catalysts in acid media; Table S2: XPS fit parameters for Ir 4f of SrFe_{0.1}Ir_{0.9}O₃ and SrIrO₃; Table S3: Approximate XPS peak positions and full width half maxes(FWHM) for SrFe_{0.1}Ir_{0.9}O₃ after 10 h stability measurement; Table S4: Stability number (S-number) of different catalysts. Refs. [22,24,32,42–50] are cited in the supplementary materials.

Author Contributions: Conceptualization, M.L. and W.Z.; methodology, M.L. and J.D.; formal analysis, M.L., J.D., and T.W.; investigation, M.L. and T.W.; writing—original draft preparation, M.L.; writing—review and editing, M.L., T.W., and W.Z.; supervision, T.W. and W.Z. All authors have read and agreed to the published version of the manuscript.

Funding: This work was supported by the National Natural Science Foundation of China (no. 11974099), Plan for Leading Talent of Fundamental Research of the Central China in 2020, the Program for Science and Technology Innovation Talents in Universities of Henan Province (grant no. 20HASTIT028), the Natural Science Foundation of Henan Province (grant no. 202300410068), and the Postdoctoral Foundation of Henan Province (201902029).

Informed Consent Statement: Informed consent was obtained from all subjects involved in the study.

Data Availability Statement: The data that support the findings of this study are available from the corresponding authors upon reasonable request.

Conflicts of Interest: The authors declare no competing financial interest.

References

1. Suen, N.T.; Hung, S.F.; Quan, Q.; Zhang, N.; Xu, Y.J.; Chen, H.M. Electrocatalysis for the oxygen evolution reaction: Recent development and future perspectives. *Chem. Soc. Rev.* **2017**, *46*, 337–365. [\[CrossRef\]](#)
2. Turner, J.A. Sustainable hydrogen production. *Science* **2004**, *305*, 972–974. [\[CrossRef\]](#)
3. Bodner, M.; Hofer, A.; Hacker, V. H₂ generation from alkaline electrolyzer. *Wiley Interdiscip. Rev. Energy Environ.* **2015**, *4*, 365–381.
4. Li, Y.; Sun, Y.; Qin, Y.; Zhang, W.; Wang, L.; Luo, M.; Yang, H.; Guo, S. Recent advances on water-splitting electrocatalysis mediated by noble-metal-based nanostructured materials. *Adv. Energy Mater.* **2020**, *10*, 1903120. [\[CrossRef\]](#)
5. You, B.; Sun, Y. Innovative strategies for electrocatalytic water splitting. *Acc. Chem. Res.* **2018**, *51*, 1571–1580. [\[CrossRef\]](#)
6. McCrory, C.C.L.; Jung, S.; Ferrer, I.M.; Chatman, S.M.; Peters, J.C.; Jaramillo, T.F. Benchmarking hydrogen evolving reaction and oxygen evolving reaction electrocatalysts for solar water splitting devices. *J. Am. Chem. Soc.* **2015**, *137*, 4347–4357. [\[CrossRef\]](#)
7. Hu, C.; Zhang, L.; Gong, J. Recent progress made in the mechanism comprehension and design of electrocatalysts for alkaline water splitting. *Energy Environ. Sci.* **2019**, *12*, 2620–2645. [\[CrossRef\]](#)
8. Wang, J.; Cui, W.; Liu, Q.; Xing, Z.; Asiri, A.M.; Sun, X. Recent progress in cobalt-based heterogeneous catalysts for electrochemical water splitting. *Adv. Mater.* **2016**, *28*, 215–230. [\[CrossRef\]](#)
9. Osgood, H.; Devaguptapu, S.V.; Xu, H.; Cho, J.; Wu, G. Transition metal (Fe, Co, Ni, and Mn) oxides for oxygen reduction and evolution bifunctional catalysts in alkaline media. *Nano Today* **2016**, *11*, 601–625. [\[CrossRef\]](#)
10. Dotan, H.; Landman, A.; Sheehan, S.W.; Malviya, K.D.; Shter, G.E.; Grave, D.A.; Arzi, Z.; Yehudai, N.; Halabi, M.; Gal, N.; et al. Decoupled hydrogen and oxygen evolution by a two-step electrochemical-chemical cycle for efficient overall water splitting. *Nat. Energy* **2019**, *4*, 786–795. [\[CrossRef\]](#)
11. Zhang, B.; Zheng, X.; Voznyy, O.; Comin, R.; Bajdich, M.; García-Melchor, M.; Han, L.; Xu, J.; Liu, M.; Zheng, L.; et al. Homogeneously dispersed multimetal oxygen-evolving catalysts. *Science* **2016**, *352*, 333–337. [\[CrossRef\]](#)
12. Dionigi, F.; Strasser, P. NiFe-Based (Oxy)Hydroxide catalysts for oxygen evolution reaction in non-acidic electrolytes. *Adv. Energy Mater.* **2016**, *6*, 1600621. [\[CrossRef\]](#)
13. McCrory, C.C.L.; Jung, S.; Peters, J.C.; Jaramillo, T.F. Benchmarking heterogeneous electrocatalysts for the oxygen evolution reaction. *J. Am. Chem. Soc.* **2013**, *135*, 16977–16987. [\[CrossRef\]](#)
14. Fabbri, E.; Schmidt, T.J. Oxygen evolution reaction—The enigma in water electrolysis. *ACS Catal.* **2018**, *8*, 9765–9774. [\[CrossRef\]](#)
15. Feng, J.; Lv, F.; Zhang, W.; Li, P.; Wang, K.; Yang, C.; Wang, B.; Yang, Y.; Zhou, J.; Lin, F.; et al. Iridium-based multimetallic porous hollow nanocrystals for efficient overall-water-splitting catalysis. *Adv. Mater.* **2017**, *29*, 1–8. [\[CrossRef\]](#)
16. Xu, X.; Shao, Z.; Jiang, S.P. High-entropy materials for water electrolysis. *Energy Technol.* **2022**, *10*, 1–17. [\[CrossRef\]](#)
17. Sun, H.; Song, S.; Xu, X.; Dai, J.; Yu, J.; Zhou, W.; Jung, W. Recent progress on structurally ordered materials for electrocatalysis. *Adv. Energy Mater.* **2021**, *11*, 2101937. [\[CrossRef\]](#)
18. Xu, X.; Wang, W.; Zhou, W.; Shao, Z. Recent advances in novel nanostructuring methods of perovskite electrocatalysts for energy-related applications. *Small Methods* **2018**, *2*, 1800071. [\[CrossRef\]](#)
19. Hwang, J.; Rao, R.R.; Giordano, L.; Katayama, Y.; Yu, Y.; Shao-horn, Y. Perovskites in catalysis and electrocatalysis. *Science* **2017**, *358*, 751–756. [\[CrossRef\]](#)
20. Hwang, J.; Feng, Z.; Charles, N.; Wang, X.R.; Lee, D.; Stoerzinger, K.A.; Shao-Horn, Y. Tuning perovskite oxides by strain: Electronic structure, properties, and functions in (electro)catalysis and ferroelectricity. *Mater. Today* **2019**, *31*, 100–118. [\[CrossRef\]](#)
21. Khan, R.; Mehran, M.T.; Naqvi, S.R.; Khoja, A.H.; Mahmood, K.; Shahzad, F.; Hussain, S. Role of perovskites as a Bi-functional catalyst for electrochemical water splitting: A review. *Int. J. Energy Res.* **2020**, *44*, 9714–9747. [\[CrossRef\]](#)
22. Seitz, L.C.; Dickens, C.F.; Nishio, K.; Hikita, Y.; Montoya, J.; Doyle, A.; Kirk, C.; Vojvodic, A.; Hwang, H.Y.; Norskov, J.K. A highly active and stable IrO_x/SrIrO₃ catalyst for the oxygen evolution reaction. *Science* **2016**, *353*, 1011–1014. [\[CrossRef\]](#)
23. Wen, Y.; Liu, C.; Huang, R.; Zhang, H.; Li, X.; García de Arquer, F.P.; Zhang, B. Introducing Brønsted acid sites to accelerate the bridging-oxygen-assisted deprotonation in acidic water oxidation. *Nat. Commun.* **2022**, *13*, 4871. [\[CrossRef\]](#)
24. Yang, L.; Chen, H.; Shi, L.; Li, X.; Chu, X.; Chen, W.; Li, N.; Zou, X. Enhanced iridium mass activity of 6h-phase, ir-based perovskite with nonprecious incorporation for acidic oxygen evolution electrocatalysis. *ACS Appl. Mater. Interfaces* **2019**, *11*, 42006–42013. [\[CrossRef\]](#)
25. Yang, L.; Yu, G.; Ai, X.; Yan, W.; Duan, H.; Chen, W.; Li, X.; Wang, T.; Zhang, C.; Huang, X.; et al. Efficient oxygen evolution electrocatalysis in acid by a perovskite with face-sharing IrO₆ octahedral dimers. *Nat. Commun.* **2018**, *9*, 1–9. [\[CrossRef\]](#)
26. Jin, H.; Liu, X.; Vasileff, A.; Jiao, Y.; Zhao, Y.; Zheng, Y.; Qiao, S.Z. Single-crystal nitrogen-rich two-dimensional Mo₅N₆ nanosheets for efficient and stable seawater splitting. *Acs Nano* **2018**, *12*, 12761–12769. [\[CrossRef\]](#)
27. Grosvenor, A.P.; Kobe, B.A.; McIntyre, N.S. Studies of the oxidation of iron by water vapour using X-ray photoelectron spectroscopy and QUASES™. *Surf. Sci.* **2004**, *572*, 217–227. [\[CrossRef\]](#)
28. Reiera, T.; Teschner, D.; Lunkenbein, T.; Bergmann, A.; Selvec, S.; Kraehnert, R.; Schlögl, R.; Strasser, P. Electrocatalytic oxygen evolution on iridium oxide: Uncovering catalyst-substrate interactions and active iridium oxide species. *J. Electrochem. Soc.* **2014**, *161*, F876. [\[CrossRef\]](#)
29. Pfeifer, V.; Jones, T.E.; Wrabetz, S.; Massué, C.; Velasco Vélez, J.J.; Arrigo, R.; Scherzer, M.; Piccinin, S.; Hävecker, M.; Knop-Gericke, A.; et al. Reactive oxygen species in iridium-based OER catalysts. *Chem. Sci.* **2016**, *7*, 6791–6795. [\[CrossRef\]](#)

30. Wang, Y.; Zhou, T.; Jiang, K.; Da, P.; Peng, Z.; Tang, J.; Kong, B.; Cai, W.; Yang, Z.; Zheng, G. Reduced mesoporous Co_3O_4 nanowires as efficient water oxidation electrocatalysts and supercapacitor electrodes. *Adv. Energy Mater.* **2014**, *4*, 1400696. [[CrossRef](#)]
31. Nong, H.N.; Reier, T.; Oh, H.; Gliech, M.; Paciok, P.; Vu, T.H.; Teschner, D.; Heggen, M.; Petkov, V.; Schlögl, R.; et al. A unique oxygen ligand environment facilitates water oxidation in hole-doped IrNiO_x core-shell electrocatalysts. *Nat. Catal.* **2018**, *1*, 841–851. [[CrossRef](#)]
32. Grimaud, A.; Demortière, A.; Saubanère, M.; Dachraoui, W.; Duchamp, M.; Doublet, M.; Tarascon, J.M. Activation of surface oxygen sites on an iridium-based model catalyst for the oxygen evolution reaction. *Nat. Energy* **2016**, *2*, 1–10. [[CrossRef](#)]
33. Seki, H.; Hosaka, Y.; Saito, T.; Mizumaki, M.; Shimakawa, Y. Ferromagnetism induced by substitution of the iron (IV) ion by an unusual high-valence nickel (IV) ion in antiferromagnetic SrFeO_3 . *Angew. Chem. Int. Ed.* **2016**, *128*, 1382–1385. [[CrossRef](#)]
34. Petrie, J.R.; Jeen, H.; Barron, S.C.; Meyer, T.L.; Lee, H. Enhancing perovskite electrocatalysis through strain tuning of the oxygen deficiency. *J. Am. Chem. Soc.* **2016**, *138*, 7252–7255. [[CrossRef](#)]
35. Calle-Vallejo, F.; Inoglu, N.G.; Su, Y.; Martínez, J.I.; Man, I.C.; Koper, M.T.M.; Kitchin, J.R.; Rossmeisl, J. Number of outer electrons as descriptor for adsorption processes on transition metals and their oxides. *Chem. Sci.* **2013**, *4*, 1245–1249. [[CrossRef](#)]
36. Diaz-Morales, O.; Ledezma-Yanez, I.; Koper, M.T.M. Guidelines for the rational design of Ni-based double hydroxide electrocatalysts for the oxygen evolution reaction. *ACS Catal.* **2015**, *5*, 5380–5387. [[CrossRef](#)]
37. Ma, C.; Sun, W.; Qamar, W.; Zhou, Z.; Zhang, H.; Shen, Q.; Cao, L.; Yang, J. Lanthanides regulated the amorphization-crystallization of IrO_2 for outstanding OER performance. *ACS Appl. Mater. Interfaces* **2020**, *12*, 34980–34989. [[CrossRef](#)]
38. Chen, J.; Cui, P.; Zhao, G.; Rui, K.; Lao, M.; Chen, Y.; Zheng, X.; Jiang, Y.; Pan, H.; Dou, S.X.; et al. Low-coordinate iridium oxide confined on graphitic carbon nitride for highly efficient oxygen evolution. *Angew. Chem. Int. Ed.* **2019**, *58*, 12540–12544. [[CrossRef](#)]
39. Sen, F.G.; Kinaci, A.; Narayanan, B.; Gray, S.K.; Davis, M.J.; Sankaranarayanan, S.K.; Chan, M.K. Towards accurate prediction of catalytic activity in IrO_2 nanoclusters via first principles-based variable charge force field. *J. Mater. Chem. A* **2015**, *3*, 18970–18982. [[CrossRef](#)]
40. Wen, Y.; Chen, P.; Wang, L.; Li, S.; Wang, Z.; Abed, J.; Sargent, E.H. Stabilizing highly active Ru sites by suppressing lattice oxygen participation in acidic water oxidation. *J. Am. Chem. Soc.* **2021**, *143*, 6482–6490. [[CrossRef](#)]
41. Hu, J. Oxygen evolution reaction on IrO_2 -based DSA[®] type electrodes: Kinetics analysis of Tafel lines and EIS. *Int. J. Hydrog. Energy* **2004**, *29*, 791–797. [[CrossRef](#)]
42. Gao, R.; Zhang, Q.; Chen, H.; Chu, X.; Li, G.D.; Zou, X. Efficient acidic oxygen evolution reaction electrocatalyzed by iridium-based 12L-perovskites comprising trinuclear face-shared IrO_6 octahedral strings. *J. Energy Chem.* **2020**, *47*, 291–298. [[CrossRef](#)]
43. Diaz-Morales, O.; Raaijman, S.; Kortlever, R.; Kooyman, P.J.; Wezendonk, T.; Gascon, J.; Koper, M.T. Iridium-based double perovskites for efficient water oxidation in acid media. *Nat. Commun.* **2016**, *7*, 1–6. [[CrossRef](#)]
44. Retuerto, M.; Pascual, L.; Piqué, O.; Kayser, P.; Salam, M.A.; Mokhtar, M.; Rojas, S. How oxidation state and lattice distortion influence the oxygen evolution activity in acid of iridium double perovskites. *J. Mater. Chem. A* **2021**, *9*, 2980–2990. [[CrossRef](#)]
45. Edgington, J.; Schweitzer, N.; Alayoglu, S.; Seitz, L.C. Constant Change: Exploring Dynamic Oxygen Evolution Reaction Catalysis and Material Transformations in Strontium Zinc Iridate Perovskite in Acid. *J. Am. Chem. Soc.* **2021**, *143*, 9961–9971. [[CrossRef](#)]
46. Chen, Y.; Li, H.; Wang, J.; Du, Y.; Xi, S.; Sun, Y.; Xu, Z.J. Exceptionally active iridium evolved from a pseudo-cubic perovskite for oxygen evolution in acid. *Nat. Commun.* **2019**, *10*, 1–10. [[CrossRef](#)]
47. Shang, C.; Cao, C.; Yu, D.; Yan, Y.; Lin, Y.; Li, H.; Zeng, J. Electron correlations engineer catalytic activity of pyrochlore iridates for acidic water oxidation. *Adv. Mater.* **2019**, *31*, 1–6. [[CrossRef](#)]
48. Chen, H.; Shi, L.; Liang, X.; Wang, L.; Asefa, T.; Zou, X. Optimization of Active Sites via Crystal Phase, Composition, and Morphology for Efficient Low-Iridium Oxygen Evolution Catalysts. *Angew. Chem. Int. Ed.* **2020**, *59*, 19654–19658. [[CrossRef](#)]
49. Liang, X.; Shi, L.; Cao, R.; Wan, G.; Yan, W.; Chen, H.; Zou, X. Perovskite-Type Solid Solution Nano-Electrocatalysts Enable Simultaneously Enhanced Activity and Stability for Oxygen Evolution. *Adv. Mater.* **2020**, *32*, 1–8. [[CrossRef](#)]
50. Miao, X.; Zhang, L.; Wu, L.; Hu, Z.; Shi, L.; Zhou, S. Quadruple perovskite ruthenate as a highly efficient catalyst for acidic water oxidation. *Nat. Commun.* **2019**, *10*, 1–7. [[CrossRef](#)]

Disclaimer/Publisher's Note: The statements, opinions and data contained in all publications are solely those of the individual author(s) and contributor(s) and not of MDPI and/or the editor(s). MDPI and/or the editor(s) disclaim responsibility for any injury to people or property resulting from any ideas, methods, instructions or products referred to in the content.